Available online at www.sciencedirect.com
ScienceDirect
Journal of Sound and Vibration 319 (2009) 199–217
JOURNAL OF SOUND AND VIBRATION
www.elsevier.com/locate/jsvi

Comparison of semi-empirical models for turbulent boundary layer wall pressure spectra

Y.F. Hwang*, William K. Bonness, Stephen A. Hambric

Applied Research Laboratory, Pennsylvania State University, State College, Pennsylvania 16804-0030, USA

Received 12 April 2007; received in revised form 29 April 2008; accepted 3 June 2008
Handling Editor: S. Bolton
Available online 22 July 2008

Abstract

This paper reviews the development of semi-empirical models which calculate the turbulent boundary layer wall pressure frequency spectra. Various models published from the late 1960s to 2004 are reviewed, and the pressure spectra calculated using these models are compared to measured data obtained at various flow conditions at a substantially wide range of Reynolds number and boundary layer thickness. The experimental data consists of flows on flat surfaces in air and cylindrical surfaces in water. A summary of the results on the applicability and limitation of each of the models compared is discussed. A model is identified that provides a good overall prediction of the frequency spectra for all cases evaluated. The readers may use the information presented to choose a model appropriate for their specific applications.

1. Introduction

Analyses of the structural response to the pressure fluctuations of turbulent boundary layer (TBL) flows have been investigated extensively over the past 50 years. The spatial and temporal characteristics of the forcing function are usually expressed in terms of a second moment of the pressure field statistics, such as the space–time correlation function or its Fourier conjugate, the wavevector-frequency spectrum. The partial (temporal) Fourier transform of the space–time correlation function, the cross-spectral density function, is also frequently used. Research on the wavenumber-frequency spectrum prior to 1996 was comprehensively reviewed by Bull [1].

When the Corcos-type cross-spectrum [1,2] or its corresponding wavevector-frequency spectrum is used to model a homogeneous turbulent flow, the point frequency spectrum, $\phi_p(\omega)$, is uniform in space and is the common separable factor from either the cross-spectral term or the wavevector term. That is, the wavenumber-frequency spectrum $\Phi_p(k_1,k_3,\omega)$ on the wavevector plane $\mathbf{k} = (k_1,k_3)$ can be expressed as [3]

$$\Phi_p(k_1,k_3,\omega) = \phi_p(\omega)(U_c/\omega)^2 f(\tilde{k}_1,\tilde{k}_3), \tag{1}$$

*Corresponding author. Current address: Electroacoustic Graduate Program, Feng Chia University, Taichung, Taiwan 40724, ROC. Tel.: +886 4 2451 7250x6304; fax: +886 4 2451 7110.
E-mail address: yfhwang@fcu.edu.tw (Y.F. Hwang).

0022-460X/$ - see front matter © 2008 Elsevier Ltd. All rights reserved.
doi:10.1016/j.jsv.2008.06.002

where k_1 and k_3 are the streamwise and spanwise wavenumber, U_c is the convection velocity, $\tilde{k}_1(=k_1U_c/\omega)$ and $\tilde{k}_3(=k_3U_c/\omega)$ are the dimensionless wavenumbers, and $f(\tilde{k}_1,\tilde{k}_3)$ is a normalized dimensionless wavevector spectrum. Since $\Phi_p(k_1,k_3,\omega)$ is the Fourier transform of the space–time correlation function, by definition [1,3],

$$\phi_p(\omega)=\int_{-\infty}^{\infty}\int_{-\infty}^{\infty}\Phi_p(k_1,k_3,\omega)\,\mathrm{d}k_1\,\mathrm{d}k_3 \tag{2}$$

and

$$\int_{-\infty}^{\infty}\int_{-\infty}^{\infty}f(\tilde{k}_1,\tilde{k}_3)\,\mathrm{d}\tilde{k}_1\,\mathrm{d}\tilde{k}_3=1. \tag{3}$$

In this paper $\phi_p(\omega)$ is considered to be a double-sided spectrum, and the mean square pressure $\langle p^2\rangle$ is, therefore, the integrated sum of $\phi_p(\omega)$ over ω from $-\infty$ to ∞. In the case of the Corcos spectrum,

$$f(\tilde{k}_1,\tilde{k}_3)=(\alpha_1\alpha_3/\pi^2)/\{[\alpha_1^2+(1-\tilde{k}_1)^2][\alpha_3^2+\tilde{k}_3^2]\}, \tag{4}$$

where the constants α_1 and α_3 are the longitudinal and lateral decay rates of the correlation, which typically range from 0.10 to 0.12 and 0.7 to 1.2, respectively. This spectrum has a peak value of $(\alpha_1\alpha_3\pi^2)^{-1}$, which occurs at $(\tilde{k}_1,\tilde{k}_3)=(1,0)$, or at $(k_1,k_3)=(k_c,0)$, where $k_c(=\omega/U_c)$ is the convection wavenumber. The spectral value at $(\tilde{k}_1,\tilde{k}_3)=(0,0)$ is equal to $\alpha_1/[\pi^2\alpha_3(1+\alpha_1^2)]$. Corcos's spectrum is considered to be low-wavenumber white, since there are only slight variations of the spectral levels in the low-wavenumber region, where $|(k_1,k_3)|<0.25k_c$. The ratio between Corcos's low-wavenumber spectrum and the spectral peak value in the convective ridge is about $\alpha_1^2/(1+\alpha_1^2)\approx 0.01$, which is about two orders of magnitude larger than the values reported from experiments [4].

In a study to determine the effects of different models of the wavenumber-frequency spectra on sound radiated by turbulent boundary layer driven rectangular plates, Graham [3] used several models of $f(\tilde{k}_1,\tilde{k}_3)$ in his analysis. Although the radiated sound power from a structure is proportional to the forcing point frequency spectrum, $\phi_p(\omega)$, Graham's sound powers were normalized by it. Therefore, the effect of the different choice of models for $\phi_p(\omega)$ was not discussed by Graham. This paper compares various models for the determination of $\phi_p(\omega)$, which is also critical for computing the actual sound power using the method presented by Graham and others.

Traditionally, the frequency spectrum is determined from empirical curves plotted according to certain scaling laws, where the dimensionless spectral density is represented as a function of dimensionless frequency. For example, $\phi_p(\omega)U_\infty/q^2\delta_*$ is frequently plotted as a function of $\omega\delta_*/U_\infty$, where U_∞ is the free stream velocity, $q(=1/2\rho U_\infty^2;\ \rho=$ fluid density) is the local dynamic pressure, and δ_* is the boundary layer displacement thickness. In this example, q is used as the pressure scale, and δ_*/U_∞ as the time scale. Some earlier empirical models, e.g., the Cockburn and Robertson [5] model, reflect data expressed in these scales.

Wall shear stress, τ_w, is more frequently used as a pressure scaling factor in conjunction with δ_*/U_∞, δ/U_∞, δ_*/u_*, δ/u_* or ν/u_*^2 as the time scale (where δ is the boundary layer thickness, $u_*=\sqrt{\tau_w/\rho}$ is the friction velocity, and ν is the kinematic coefficient of viscosity). Scaling issues have been elaborately discussed by Blake [4], Farabee and Casarella [6], Keith et al. [7], Bull [1], Smol'yakov [8], Goody [9], and others. There is no single scaling that leads to a satisfactory collapse of experimental data at all pertinent frequencies. According to the work of the above authors, the use of different scales to collapse data in different frequency regions are shown in Fig. 1 and summarized as follows:

(1) In the low-frequency region, $\omega\delta_*/U_\infty\leqslant 0.03$ (or $\omega\delta/u_*\leqslant 5$), the spectrum varies as ω^2. Either q or τ_w may be used as the pressure scale, and δ_*/U_∞ is used as the time scale, e.g., $\phi_p(\omega)U_\infty/q^2\delta_*=f_1(\omega\delta_*/U_\infty)=\text{constant}\times(\omega\delta_*/U_\infty)^2$.
(2) In the mid-frequency region, $5\leqslant\omega\delta/u_*\leqslant 100$, which includes the spectral peak occurring approximately at $\omega\delta/u_*=50$; τ_w is used as the pressure scale and δ/u_* as the time scale; e.g., $\phi_p(\omega)u_*/\tau_w^2\delta=f_2(\omega\delta/u_*)$.
(3) The universal range (or overlap region), $100\leqslant\omega\delta/u_*\leqslant 0.3(u_*\delta/\nu)$, exists when Reynolds number $u_*\delta/\nu>333$ (or $R_\theta\geqslant 3500$ according to Smol'yakov [8], where $R_\theta=U_\infty\delta_\theta/\nu$, $\delta_\theta=$ momentum thickness). Both inner- and outer-layer scaling can be used to make the data collapse, i.e., $\omega\phi_p(\omega)\tau_w{}^2=f_3=$ constant. This implies

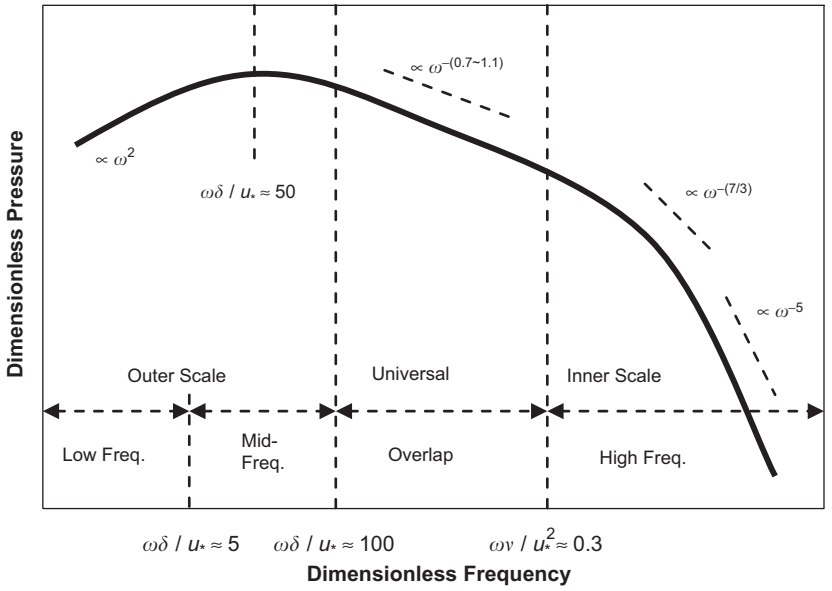

Fig. 1. General spectral characteristics of a TBL wall pressure spectrum at various frequency regions.

$\phi_p(\omega)$ varies as ω^{-1} in this range, but recent data analyzed by Goody [9] and Smol'yakov [8] show it may vary as $\omega^{-0.7}$ and $\omega^{-1.11}$, respectively.

(4) In the high-frequency region, $0.3 \leqslant \omega\nu/u_*^2$, the spectrum is influenced by viscosity and scaled on inner-layer variables. Usually, τ_w is used as the pressure scale and ν/u_*^2 as the time scale, e.g., $\phi_p(\omega)u_*^2/\tau_w^2\nu = f_4(\omega\nu/u_*^2)$ (the spectrum varies from ω^{-1} to ω^{-5}).

These distinct spectral characteristics are depicted in Fig. 1, which indicates that a suitable descriptive model must be a function of multiple scaled variables, which will predominantly behave as $f_i(i = 1, 2, 3, 4)$ in each of the four regions of frequencies. Semi-empirical models for calculating the frequency spectrum have been proposed by several investigators. The reason for using the term "semi-empirical models" is because all models discussed hereafter were fitted empirically with some degree of theoretical guidance. The earlier models by Maestrello [10], Cockburn and Robertson [5] and Efimtsov [11] are single scale models. A later Efimtsov model [12] may be considered as a multiple scale model since it includes a Reynolds number dependency. The more comprehensive multiple scale models were published recently by Smol'yakov [8] and Goody [9]. This paper provides an overview on the progress of model development and compares some of these models, in terms of their similarities, differences and limitations in predicting spectral behavior and level, using measured data as a reference. Data obtained at various flow conditions (flows on flat surfaces in air and cylindrical surfaces in water at a substantially wide range of Reynolds number and boundary layer thickness) will be used.

Nine semi-empirical models are chosen for comparison in the following section although several are paired in their discussion because of similarities:

(1) Maestrello [10] model (1969)
(2) Cockburn–Robertson [5] and Efimtsov [12] models (1974 and 1984, respectively)
(3) Witting [13] model (1986)
(4) Chase [14] and Chase–Howe models [15,16] (1980 and 1987, respectively)
(5) Smol'yakov–Tkachenko [17] and Smol'yakov [8] models (1991 and 2000, respectively)
(6) Goody [9] model (2004).

These models do not constitute an exhaustive list of all models in the literature; they are chosen because of their historical significance and because they are frequently referenced by other researchers. We hope this

paper provides an impartial reference for the practicing engineer regarding the relative strengths and weaknesses of the various models.

2. Models of wall pressure frequency spectrum

2.1. Maestrello model

The Maestrello [10] model is, perhaps, the earliest semi-empirical model published. This model was developed based on measurements on the side wall of a supersonic wind tunnel. The side wall window was modified to accommodate a rigid steel plate which supported the instrumentation required for measurements. Measurements were made in the region of zero pressure gradient. Conventional zirconate ceramic disks as well as capacitance transducers with diameters of 1.5 and 2.3 mm, respectively were used. Pressure data below 800 Hz were rejected due to acoustic interference in the tunnel. The data in the range between 0.8 and 200 kHz measured at Mach numbers of 1.42, 1.98, 2.99 and 3.98 were plotted in an outer variable scale, i.e., $\phi_p(\omega)U_\infty/(\langle p^2\rangle\delta)$ versus $\omega\delta/U_\infty$. The plotted data compared favorably with other published data obtained from measurements made at highly subsonic incompressible flows. An empirical model which is the best fit of the data was given as follows [10]:

$$\phi_p(\omega)U_\infty/(\langle p^2\rangle\delta)=\sum_{n=1}^{4}A_n e^{-K_n(\omega\delta/U_\infty)}, \tag{5}$$

where

$$\begin{aligned} A_1&=0.044, & K_1&=0.0578,\\ A_2&=0.075, & K_2&=0.243,\\ A_3&=-0.093, & K_3&=1.12,\\ A_4&=-0.025, & K_4&=11.57. \end{aligned}$$

These constants are used for determining the spectral peak value, which occurs at $\omega\delta/U_\infty\approx 1.5$ (or at $\omega\delta_*/U_\infty\approx 0.2$), and controlling the rate of roll-off from the peak.

2.2. Cockburn–Robertson and Efimtsov models

In an investigation of the vibration response of spacecraft shrouds to in-flight fluctuating pressures, Cockburn and Robertson [5] utilized the following empirical equation, expressed in outer variable scaling, for the frequency spectrum of wall pressures at transonic and supersonic speeds:

$$\frac{\phi_p(f)U_\infty}{q_\infty^2\delta}=\frac{\langle p^2\rangle/q_\infty^2}{(\delta f_0/U_\infty)[1+(f/f_0)^{0.9}]^2}, \tag{6}$$

where $\langle p^2\rangle\approx[0.006/(1+0.14M^2)q_\infty]^2$, f is the circular frequency, M the local Mach number and f_0 the characteristic frequency: $f_0=0.346\ U_\infty/\delta$. The spectrum has a maximum at zero frequency and it drops off faster when frequencies exceed f_0. Mach number affects only the mean square pressure and this effect becomes insignificant at transonic and lower speeds. At high frequencies (when $f\gg f_0$), Cockburn and Robertson's model varies as $\omega^{-1.8}$, which is quite different from the spectral characteristics shown in Fig. 1.

Based on the exhaustive experimental data available from measurements of wall pressure fluctuations in zero-pressure gradient turbulent boundary layers on aircrafts in wind tunnels, Efimtsov [12] proposed the following Reynolds number dependent model for the single-sided frequency spectrum:

$$\phi_p(\omega)/(\rho^2u_*^3\delta)=\alpha\beta[(1+8\alpha^3\,Sh^2)^{1/3}+\alpha\beta\,Re(Sh/Re)^{10/3}]^{-1}, \tag{7}$$

where, $\alpha=0.01$, $Re=\delta u_*/\nu$, $\beta=[1+(3000/Re)^3]^{1/3}$ and $Sh=\omega\delta/u_*$. Unlike his previous model [11] which is valid only for $\omega\delta/u_*<1.3Re^{7/8}$, the new model is valid for all practical range of Re. Obviously, at high frequencies, the predicted spectra will decrease $\propto\omega^{-10/3}$.

2.3. Witting model

Witting [13] developed a theoretical wavenumber-frequency spectral model based on a stochastic model of turbulent burst/sweep events, where he considered each burst and sweep as an independent event and as a dipole that moves with the local mean flow. He derived a Bernoulli relationship that connects the wall fluctuating pressure from an individual event to the fluctuating velocity. Based on the result of Fourier analysis, he assumed a form of the wall pressure wavevector-frequency spectrum contributed by the fluctuating velocity at a distance, d, from the wall. The overall wavenumber-frequency spectrum is then obtained by summing, according to an assumed probability density function, over a range of d: from the inner length scale $\delta_{\min}$ to the outer length scale $\delta_{\max}$, where $\delta_{\min}$ and $\delta_{\max}$ may be expressed as a constant ratio to δ_*, e.g., $\delta_{\min}=0.1\delta_*$ and $\delta_{\max}=4\delta_*$. The frequency spectrum is then obtained by integrating the wavenumber-frequency spectrum over the wavevector plane:

$$\phi_p(\omega)=\frac{(16/3\pi)\langle p\rangle^2}{|\omega|[1+2/(3C^2)]\ln(\delta_{\max}/\delta_{\min})}\int_{\omega\delta_{\min}/U_c}^{\omega\delta_{\max}/U_c}x^3K_1(2x)\,\mathrm{d}x \tag{8}$$

where $\langle p^2\rangle=0.015\rho^2U_c^2u_*^2$ is the mean square pressure, $C=8$, and K_1 is a modified Bessel function. Witting's model is not a simple semi-empirical model. The spectrum is an integral of a special function with frequency-dependent integration limits. As will be shown later, Witting's model reflects the spectral features similar to those shown in Fig. 1.

2.4. Chase and Chase–Howe models

A comprehensive descriptive semi-empirical model for wavenumber-frequency spectrum was published by Chase [14]. This model was further improved in a follow-up paper by the same author [15]. The Chase frequency spectrum, $\phi_p(\omega)$, is obtained by integrating his wavenumber-frequency spectrum over the wavevector plane according to Eq. (2). The latest version [15] of the frequency spectrum is expressed as follows:

$$\phi_p(\omega)=\rho^2u_*^4\omega^{-1}[a_+\gamma_M\alpha_M^{-3}(1+\mu_M^2\alpha_M^2)+3\pi C_T\alpha_T^{-1}(1+\alpha_T^{-2})], \tag{9}$$

where $\alpha_M^2=\alpha_T^2=1+(b\omega\delta/U_c)^{-2}$, $C_M=0.1553$, $C_T=0.00476$, $b=0.75$, $\mu_M=0.176$, $a_+=2\pi(C_M+C_T)$ and $\gamma_M=C_M/(C_M+C_T)$. At the low-frequency limit, this spectrum approaches a constant rather than varying as ω^2.

A similar version of Chase's model [15] was presented by Howe [16] in a rather concise manner, i.e.,

$$\phi_p(\omega)=\rho^2u_*^4\omega^{-1}(\omega\delta_*/U_\infty)^3[\alpha_p^2+(\omega\delta_*/U_\infty)^2]^{-3/2},\quad \alpha_p=0.12. \tag{10}$$

This spectrum, unlike that in Eq. (9), is proportional to ω^2 at low frequencies. Eq. (10) is the so-called Chase–Howe model (Goody [9]). However, both the Chase and Chase–Howe spectra vary as ω^{-1} at high frequencies (universal range and beyond). The integration of Eqs. (9) and (10) over ω from $-\infty$ to ∞ diverges and does not yield the mean square pressure. Since these models do not decay faster than ω^{-1}, such as $\omega^{-7/3}$ or ω^{-5}, at high frequencies, their applicability is apparently limited to frequencies near or below the universal range cutoff, i.e., $\omega\nu/u_*^2\leqslant 0.3$.

According to the form presented by Howe [16], the normalized Chase [15] wavevector-frequency spectrum in the hydrodynamic domain ($|k|\geqslant\omega/c$; $c=$ speed of sound), can be expressed as follows:

$$\begin{aligned}f(\tilde{k}_1,\tilde{k}_3)=&[\phi_p(\omega)]^{-1}(U_c/u_*)[\beta^2(1-\tilde{k}_1)^2+\tilde{k}^2+(b\omega\delta/U_c)^{-2}]^{-5/2}\\&\times\left[C_M\tilde{k}_1^2+C_T\tilde{k}^2\frac{\beta^2(1-\tilde{k}_1)^2+\tilde{k}^2+(b\omega\delta/U_c)^{-2}}{\tilde{k}^2+(b\omega\delta/U_c)^{-2}}\right],\end{aligned} \tag{11}$$

where $\beta=U_c/3u_*$ and $\tilde{k}^2=\tilde{k}_1^2+\tilde{k}_3^2$. Chase's low-wavenumber spectrum varies as $\tilde{k}^2$, and becomes much lower than Corcos's spectrum when $|(k_1,k_3)|\ll k_c$ (see Graham [3]).

2.5. Smol'yakov–Tkachenko and Smol'yakov models

In a paper devoted to discussing the cross-spectra and the corresponding wavevector-frequency spectra of the turbulent pressures, Smol'yakov and Tkachenko [17] utilized the following model for their frequency spectrum:

$$\phi_p(\omega) = 5.1(\tau_w^2\delta_*/U_\infty)/[1 + 0.44(\omega\delta_*/U_\infty)^{7/3}], \tag{12}$$

which is an approximate model based on the work by Tkachenko and Marshov [18]. This model depicts a flat spectrum in the low- and mid-frequency regions in a way similar to that of Cockburn and Robertson [5], and then decays as $\omega^{-7/3}$ at high frequencies.

Independent of the model shown in Eq. (12), Smol'yakov [8] proposed a new model using different scaling variables for different frequency regions. This model was based on a thorough analysis of his theoretical model of the wavenumber-frequency spectrum and a diverse group of data reported in the literature. Three distinctive characteristic frequency ranges, determined by dimensionless frequency, $\overline{\omega} = \omega v/u_*^2$, are established for $R_\theta > 1000$:

$$\begin{aligned}
\phi_p(\omega) &= 1.49\times10^{-5}R_\theta^{2.74}\overline{\omega}^2(1 - 0.117R_\theta^{0.44}\overline{\omega}^{1/2})/[u_*^2/(\tau_w^2 v)] \\
&\quad \text{when } \overline{\omega} < \overline{\omega}_0, \\
\phi_p(\omega) &= 2.75\overline{\omega}^{-1.11}\{1 - 0.82\exp[-0.51(\overline{\omega}/\overline{\omega}_o - 1)]\}/[u_*^2/(\tau_w^2 v)] \\
&\quad \text{when } \overline{\omega}_0 < \overline{\omega} < 0.2, \\
\phi_p(\omega) &= (38.9\mathrm{e}^{-8.35\overline{\omega}} + 18.6\mathrm{e}^{-3.58\overline{\omega}} + 0.31\mathrm{e}^{-2.14\overline{\omega}}) \\
&\quad \times \{1 - 0.82\exp[-0.51(\overline{\omega}/\overline{\omega}_0 - 1)]\}/[u_*^2/(\tau_w^2 v)] \\
&\quad \text{when } \overline{\omega} > 0.2,
\end{aligned} \tag{13}$$

where $\overline{\omega}_0 = 49.35R_\theta^{-0.88}$. In the low-frequency region, $\overline{\omega} < \overline{\omega}_0$, the pressure spectrum is proportional to ω^2. In the mid-frequency region, $\overline{\omega}_0 < \overline{\omega} < 0.2$, the spectrum peaks and then rolls off to the "universal" range, where $\phi_p(\omega) \propto \omega^{-1.11}$ instead of $\phi_p(\omega) \propto \omega^{-1}$ as predicted by the Chase model. In the high-frequency region, $\overline{\omega} > 0.2$, $\phi_p(\omega)$ varies in an exponent form rather than a power-law form, although different portions of the exponent can be approximated in the power-law dependencies of the form ω^{-m} with the increase of the exponent m as frequency is increased.

2.6. Goody model

Using the Chase–Howe model [16], Eq. (10), as the starting point, Goody [9] incorporated the scaling behaviors shown in Fig. 1 and the spectral features indicated by the data obtained from seven research groups to obtain the following semi-empirical formula:

$$\frac{\phi_p(\omega)U_\infty}{\tau_w^2\delta} = \frac{C_2(\omega\delta/U_\infty)^2}{\left[(\omega\delta/U_\infty)^{0.75} + C_1\right]^{3.7} + \left[C_3R_T^{-0.57}(\omega\delta/U_\infty)\right]^7}, \tag{14}$$

where C_1, C_2 and C_3 are empirical constants, $R_T = (\delta/U_\infty)/(v/u_*^2)$ is the ratio of the outer to inner boundary layer time scale. The value of C_1 and C_3 recommended by Goody are 0.5 and 1.1, respectively. The value for $C_2 = 1.5$ which will be used here is one-half of Goody's suggested value ($C_2 = 3$) to account for the double-sided spectra used in this paper versus Goody's single-sided spectrum. The ratio between C_1 and $C_3R_T^{-0.57}$ determines the size of the universal range (overlap region), and this region may be very narrow at low Reynolds number flows, since $R_T \propto (u_*\delta/v)$. This model thus reflects the Reynolds number trends that exist in the measured data.

The spectrum represented by Eq. (14) increases as ω^2 in the lowest frequency region. After the peak region, it decays as approximately $\omega^{-0.7}$ in the middle frequency region (the universal range). In the highest frequency region, $\phi_p(\omega)$ decays as ω^{-5}. This model compares well with experimental data over a large range of Reynolds numbers, $1400 < R_\theta < 23400$. Goody claims that this model can be confidently extrapolated to flows at

Reynolds number higher than the data set surveyed, since the model is fitted (or calibrated) with a Reynolds number dependent factor, i.e., $R_T = (u_*/U_\infty)(u_*\delta/\nu)$.

3. Comparison of measured and predicted spectra

The calculated frequency spectra using the above models are the spectra that would be measured by a point sensor, which cannot be used to compare directly with the spectra measured by a finite-size pressure sensor because of the effect of spatial averaging over the sensor area. The wall pressure spectrum measured by a finite-size circular pressure sensor, $\phi_M(\omega)$, can be computed numerically (Blake [4]; Capone and Lauchle [19]) as follows:

$$\phi_M(\omega) = \int_{-\infty}^{\infty}\int_{-\infty}^{\infty} \Phi_p(k_1, k_3, \omega) H(ka)\, \mathrm{d}k_1\, \mathrm{d}k_3, \tag{15}$$

where $H(ka) = [2J_1(ka)/ka]^2$ is the wavenumber sensitivity function of a circular sensor with uniform pressure sensitivity of radius a at the wavenumber $k = \sqrt{k_1^2 + k_3^2}$. By substituting Eq. (1) into Eq. (15), the ratio between the measured and the theoretical point spectrum can be predicted by evaluating

$$\phi_M(\omega)/\phi_p(\omega) = \int_{-\infty}^{\infty}\int_{-\infty}^{\infty} f(\tilde{k}_1, \tilde{k}_3) H(ka)\, \mathrm{d}\tilde{k}_1\, \mathrm{d}\tilde{k}_3. \tag{16}$$

The ratio $\phi_M(\omega)/\phi_p(\omega)$ is the so-called Corcos attenuation factor, which is used to predict the theoretical point spectra when the spectra measured by finite sensors are given, or vice versa, to predict the spectra measured by finite sensors when the theoretical point spectra $\phi_p(\omega)$ are given.

Both Eq. (4) (the Corcos spectrum) and Eq. (11) (the Chase spectrum) may be used for calculating $\phi_M(\omega)/\phi_p(\omega)$. For all finite values of k, $H(ka) \to 1$ as $a \to 0$. This leads to no attenuation, i.e., $\phi_M(\omega)/\phi_p(\omega) = 1$ when $a = 0$, since $\int_{-\infty}^{\infty}\int_{-\infty}^{\infty} f(\tilde{k}_1, \tilde{k}_3)\, \mathrm{d}\tilde{k}_1\, \mathrm{d}\tilde{k}_3 = 1$. Therefore, when small sensors are used, the calculated $\phi_M(\omega)/\phi_p(\omega)$ at low frequencies will not be influenced significantly by the choice of model for $f(\tilde{k}_1, \tilde{k}_3)$. However, when the size of the sensor is larger or the frequency of interest is higher, the calculated $\phi_M(\omega)/\phi_p(\omega)$ will be influenced by the choice of the model due to the differences in the low-wavenumber spectra.

Fig. 2 shows the calculated values of $\phi_M(\omega)/\phi_p(\omega)$ using the Corcos and Chase models for circular sensors of 1 mm and 1 cm diameter. Also shown are the attenuation factors extrapolated from the data tabulated by

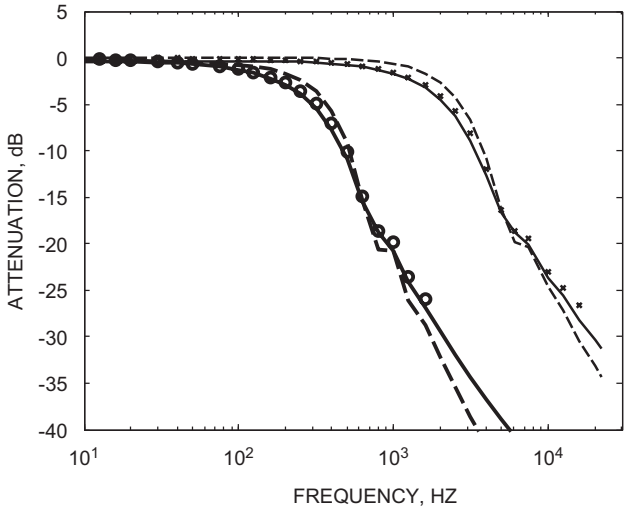

Fig. 2. Calculated attenuation, $\phi_M(\omega)/\phi_p(\omega)$, by circular sensors of 1 mm, and 1 cm diameter using Corcos's and Chase's models (also shown are data obtained from Corcos's [2] tabulated values). (——) 1 mm sensor and Corcos's model, (– – – –) 1 mm sensor and Chase's model, (✖) 1 mm sensor and Corcos's table, (——) 1 cm sensor and Corcos's model, (– – –) 1 cm sensor and Chase's model, (●) 1 cm sensor and Corcos's table.

Corcos [2] (shown by symbols O and x, for 1 cm and 1 mm sensors, respectively). The flow conditions used in the calculation are based on Schewe's [20] experiment, where $U_\infty = 6.3\,\text{m/s}$, $\delta = 3\,\text{cm}$, $\delta_* = 4.6\,\text{mm}$ and $u_* = 0.28\,\text{m/s}$. These conditions are used to determine the approximate frequency-dependent convection speed, $U_c(\omega) = [0.6 + 0.3\exp(-0.89\omega\delta_*/U_\infty]U_\infty$, and the wavenumber-frequency spectra. The attenuation factors calculated by using the Corcos and Chase models differ insignificantly when the frequency is low and the size of sensor is small. However, the differences become more noticeable as the frequency increases or the size of the sensor becomes larger.

In the following comparison of the measured and predicted spectra using the various semi-empirical models, the measured data are the sensor data corrected with attenuation factors. Two sets of measured data are shown: one is corrected by using Corcos's wavenumber spectral model while the other is corrected by using the Chase model. The uncorrected experimental data are also shown to indicate the amount of correction being made.

In each measurement condition, the measured and predicted spectra were determined in the actual frequency and pressure scales first and then converted to dimensionless forms: dimensionless spectra $[\phi_p(\omega)/\rho^2 U_\infty^3 \delta_*]$ versus dimensionless frequency $[\omega\delta_*/U_\infty]$. The relative differences among the spectra compared under the same flow conditions at the actual pressure and frequency units will be the same as those compared at any form of the dimensionless pressure and frequency (either in inner or outer scales) as discussed in Section 1. Although the dimensionless spectral densities and frequencies (shown in outer variable scales) used here do not universally collapse data at all frequencies under different flow conditions, they may still provide some useful cross comparison with other data published in the literature, especially in the low- and mid-frequency ranges.

3.1. Frequency spectra in air on flat surfaces

Schewe's [20] measurement of wall pressure spectra in a low-speed wind tunnel ($U_\infty = 6.3\,\text{m/s}$, $R_\theta = 1400$) serves as an example of very low Reynolds number flow. The pressure sensor used was 1 mm diameter ($a = 0.5\,\text{mm}$), and the attenuation by the sensor size is less than 3 dB in the frequency range reported ($<2\,\text{KHz}$). In the calculations, $u_* = 0.28\,\text{m/s}$, $\delta_* = 0.46\,\text{cm}$ as reported by Schewe, were used. The calculated spectra and measured data are shown in Fig. 3. In this low Reynolds number flow, the measured spectrum as shown in Fig. 3 indicates a rather narrow universal range, $0.6 \leqslant \omega\delta_*/U_\infty \leqslant 1.2$, where $\phi_p(\omega)$ decays approximately as $\omega^{-0.7}$. The decay rate increases with frequency and eventually the data show $\phi_p(\omega)$ decays as ω^{-5}.

The pressure spectra on a flat surface reported by Farabee and Casarella [6] in a wind tunnel are measured at several flow speeds. The data used here are measured at $U_\infty = 15.5\,\text{m/s}$, which is considerably higher than that of Schewe's experiment. With a special noise cancellation technique, they were able to measure the spectra for frequencies as low as 1 Hz. Their data, obtained by using a 0.79 mm diameter flush mounted pinhole microphone, are compared with predictions in Fig. 4. The boundary layer thickness ($\delta = 2.79\,\text{cm}$), displacement thickness ($\delta_* = 0.45\,\text{cm}$), friction velocity ($u_* = 0.625\,\text{m/s}$), and Reynolds number ($R_\theta = 3400$) measured by Farabee and Casarella are used in the calculation. The data reflect the spectral behaviors in all frequency regions shown in Fig. 1. In the universal range, they show roughly a $\omega^{-0.7}$ bevavior. In the high-frequency region, the sensor size correction may be slightly overestimated since the corrected data show a ω^{-4} rather than the generally believed ω^{-5} behavior.

Both data sets mentioned above by Schewe [20] and Farabee and Casarella [6] were used by Goody and Smol'yakov in the derivation of their spectral models. Although Smol'yakov [8] indicated that Farabee's data appeared in a technical report [21] were used, these same data were later published in a journal article by Farabee and Casarella [6].

3.2. Frequency spectra in water on cylindrical surfaces

Using the data obtained from underwater measurements provides an opportunity to assess the semi-empirical models at larger Reynolds number flows. The two in-water measurement cases that will be used were obtained from cylindrical surfaces aft of the axisymmetric forebodies of buoyancy propelled

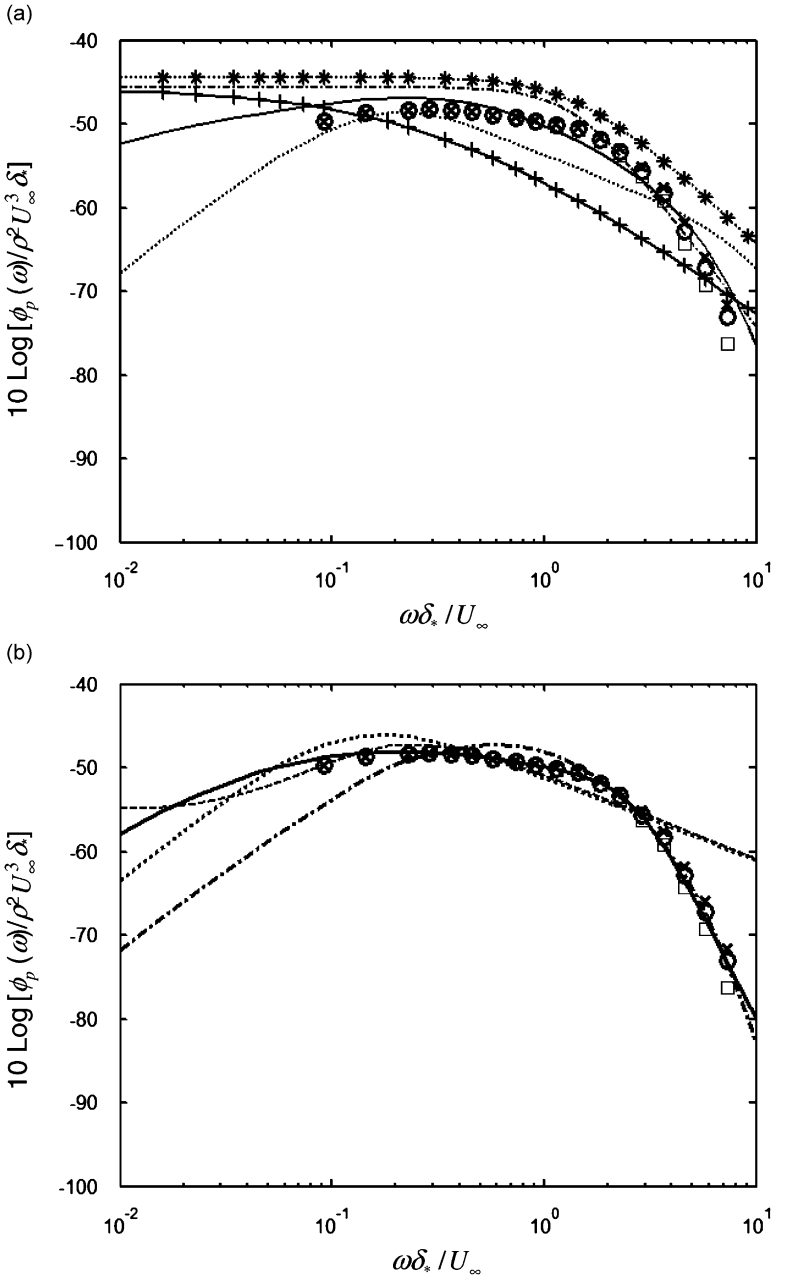

Fig. 3. Comparison of pressure spectrum measured by Schewe [20] in a wind tunnel ($R_\theta = 1400$, $\delta_* = 0.46$ cm) and predicted spectra using the semi-empirical models. (a) Predicted spectra using model by (——) Maestrello, (——+——) Cockburn–Robertson, (—·—·—) Efimtsov, (·····) Witting, (····+····) Smol'yakov–Tkachenko. (b) Predicted spectra using model by (– – – –) Chase, (▪▪▪▪▪▪▪) Chase–Howe, (▬▪▬▪▬) Smol' yakov, (——) Goody. (○) measured data corrected with Chase, (✖) measured data corrected with Corcos and (□) uncorrected measured data.

test vehicles. In the first case, transition from laminar to turbulent flow was forced at the nose region to ensure a fully developed turbulent flow at the measurement location ($R_x \approx 1.04 \times 10^7$). In this case, the measurement point is in the upstream region of the vehicle and the boundary layer is thin. In the second case, the measurement location is in the downstream region of a vehicle (the distance from the nose is about five times the diameter of the vehicle, $R_x = 7.4 \times 10^7$), where the Reynolds number is larger and the boundary layer is

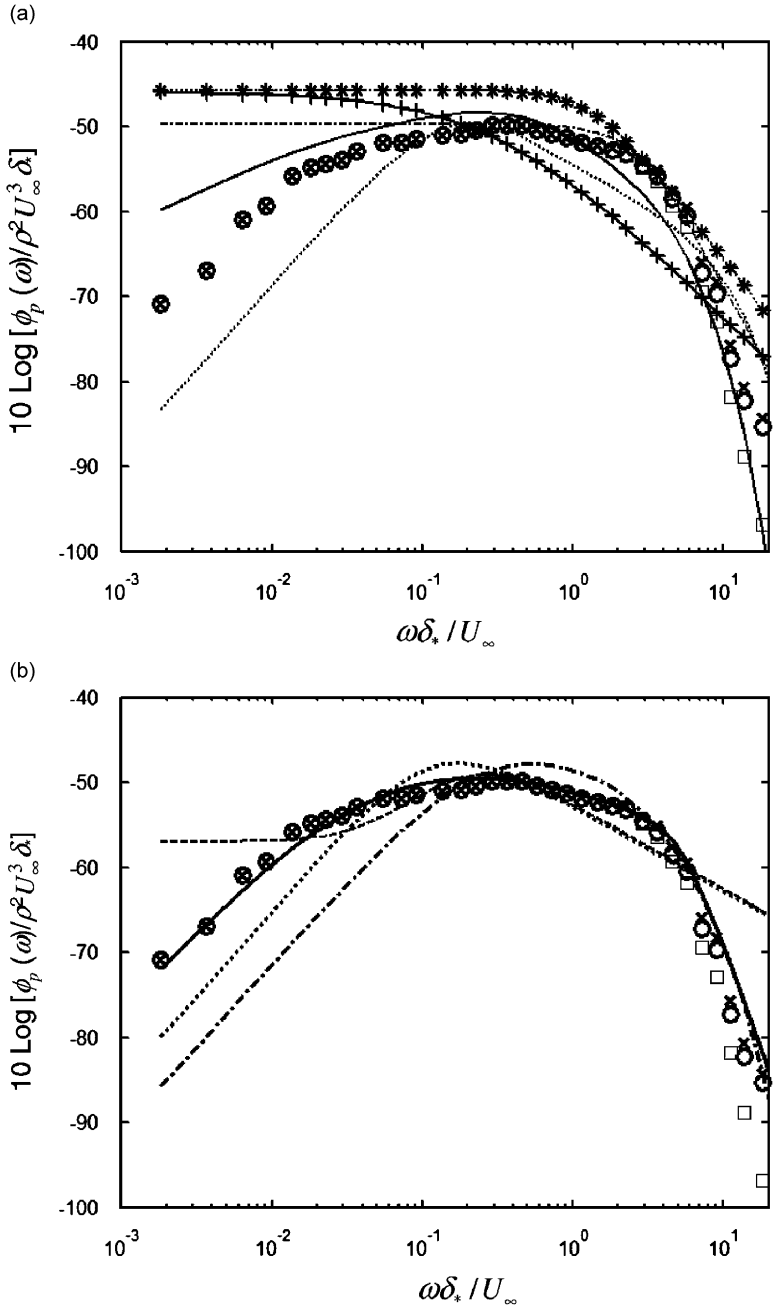

Fig. 4. Comparison of pressure spectrum measured by Farabee and Casarella [6] in a wind tunnel ($R_\theta = 3400$, $\delta_* = 0.45$ cm) and predicted spectra using the semi-empirical models. (a) Predicted spectra using model by (———) Maestrello, (———+———) Cockburn–Robertson, (—·—·—) Efimtsov, (.....) Witting, (·····+·····) Smol'yakov–Tkachenko. (b) Predicted spectra using model by (– – – –) Chase, (■ ■ ■ ■ ■) Chase–Howe, (— — —) Smol'yakov, (———) Goody. (○) the measured data corrected with Chase, (✖) measured data corrected with Corcos and (□) uncorrected measured data.

thick. These two cases, along with the two in-air cases, provide data at a wide range of Reynolds number and boundary layer thickness. Measurements of the statistical properties of the fluctuating pressures on the surfaces of this type of test vehicle were first reported by Bakewell [22]. His data compared favorably (in outer variable scaling) with data obtained from wind tunnel measurements. The schematic and operation of the vehicle were described in detail by Abarbanel et al. [23].

In the first case, the tests were conducted in a deep ocean by Galib et al. [24], where transition from laminar to turbulent flow was forced at the nose region (at the start of the contour) to ensure a fully developed turbulent flow at the location of measurement. The pressure spectra were measured with a 5 mm diameter (effective diameter = 3 mm) hydrophone at $U_\infty = 20.57$ m/s at the location where $R_x \approx 1.04 \times 10^7$ ($x = 1.25D$; where D is the diameter). In order to provide a smooth surface (to avoid surface impedance discontinuities), the hydrophone was covered by a 3.2 mm thick elastomer layer (blanket). The boundary layer displacement thickness calculated by Galib et al. using a Transitional Analysis Program System (TAPS, Gentry and Wazzan [25]) is 0.11 cm, which is close to that of 0.091 cm calculated by the flat plate equation [26]. Accordingly, other parameters such as $u_* = 0.7$ m/s, $\delta = 0.74$ cm and $\delta_\theta = 0.07$ cm calculated from the flat plate equations are believed to be sufficient for use as input parameters in the semi-empirical models.

In this measurement, the fluctuating pressures are not only attenuated by the size of the hydrophone but also by the wavenumber filtering of an external elastomer layer. The attenuation or filtering effect by such an elastomer layer, $|t(k,\omega)|^2$, is expressed as the absolute square of the ratio between the pressure on a rigid wall beneath an elastomer layer and the pressure on a rigid wall directly beneath the turbulent boundary layer. Both pressures are subject to a reference incident wave expressed in terms of an evanescent velocity potential which is launched from the boundary layer. The equation for calculating the pressure transfer function (between the surfaces of an elastomer layer) as a function of frequency and wavenumber is shown in Eq. (A.9) in the appendix, which is formulated in a way similar to the methods discussed by Chandiramani [27] and Ko and Schloemer [28]. Calculations of the measured spectra with the combined attenuations by a hydrophone and an elastomer layer are then determined by

$$\phi_M(\omega)/\phi_p(\omega) = \int_{-\infty}^{\infty}\int_{-\infty}^{\infty} f(\tilde{k}_1,\tilde{k}_3)\left|t(k,\omega)\right|^2 H(k_1,k_3)\,\mathrm{d}\tilde{k}_1\,\mathrm{d}\tilde{k}_3. \tag{17}$$

Fig. 5 shows the estimated pressure attenuations by a 0.32 cm thick elastomer blanket (using density, $\rho_e = 1050$ kg/m^3; dilatational wave speed, $c_l = 1500$ m/s; and shear wave speed, $c_s = 30$ m/s), a 0.3 cm diameter sensor, and the combined attenuations by the elastomer layer and the sensor using both the Corcos and the Chase spectra. This shows that the attenuations caused by the blanket are more severe than those by the sensor. Differences between the calculated attenuations by the two spectral models below 2.5×10^3 Hz are

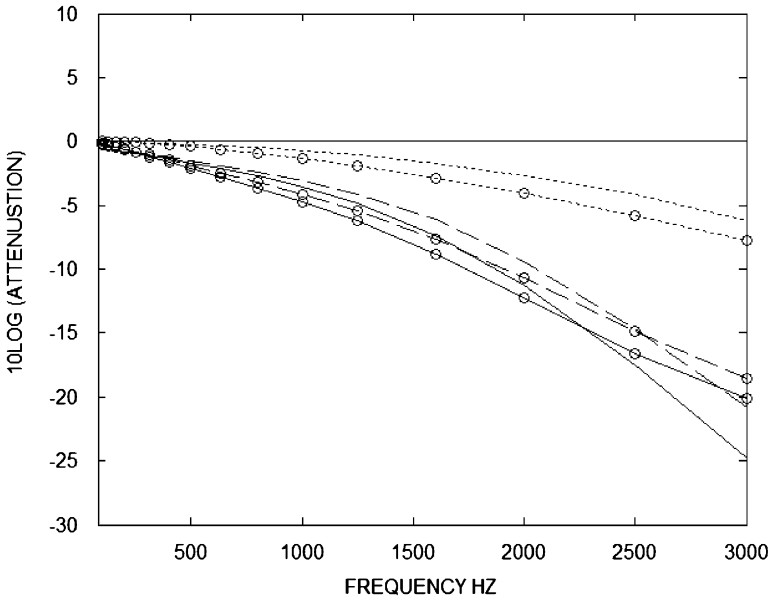

Fig. 5. The estimated pressure attenuations by a 1/8 in (3.2 mm) thick elastomer layer (blanket), a 3 mm diameter sensor, and the combined attenuations by the blanket and the sensor using both the Corcos and Chase wavenumber-frequency spectra. Attenuations when Corcos's model is used: (- - - - -) sensor only, (– –) blanket only, (—) combination of sensor and blanket. Attenuations when Chase's model is used: (- -○- -) sensor only, (—○ –) blanket only and (—○—) combination of sensor and blanket.

generally within 2–3 dB. Above 2.5×10^3 Hz the differences are on the order of 5 dB. Fig. 6 shows the comparison between spectra predicted from the empirical models and that from measured data corrected with the combined attenuations. The range of these data is not broad. However, it does cover the spectrum in the peak region, and small portions of the low- and mid-frequency regions. The higher frequency region of the underwater data will be covered in the next case.

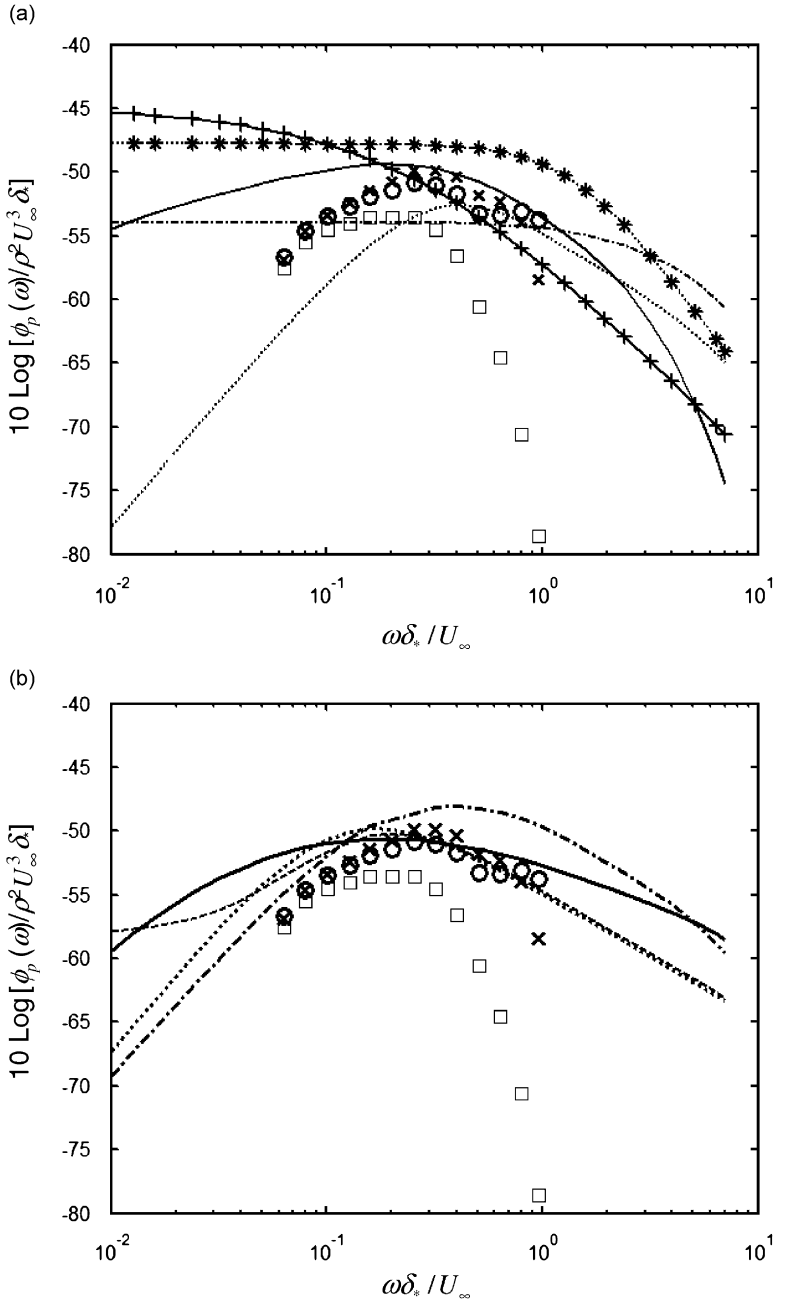

Fig. 6. Comparison of the underwater pressure spectrum measured by Galib et al. [24] on a cylindrical surface ($R_x = 1.04 \times 10^7$, $\delta_* = 0.1$ cm) and predicted spectra calculated from the semi-empirical models. (a) Predicted spectra using model by (———) Maestrello, (—+—) Cockburn–Robertson, (—·—·—) Efimtsov, (·····) Witting and (···✚···) Smol'yakov–Tkachenko. (b) Predicted spectra using model by (– – – –) Chase, (▪▪▪▪▪▪▪) Chase–Howe, (▬▪▬▪▬) Smol'yakov, (———) Goody. (○) the measured data corrected with Chase, (✖) measured data corrected with Corcos and (□) uncorrected measured data.

The second underwater case were data measured on a larger vehicle much further downstream (where $x \approx 5D$, $U_\infty = 12.86\,\text{m/s}$, $R_x = 7.8 \times 10^7$) with a 2.54 mm diameter flush mounted hydrophone (without an elastomer layer). The measured spectra were used to monitor the TBL characteristics in a conformal array experiment reported by Sherman et al. [29]. In this case, the boundary layer parameters are not known. The location of transition from laminar to turbulent flow is estimated (according to Casarella et al. [30]) to be approximately $x \approx D/2 (R_x \approx 7.8 \times 10^6)$, which represents about 10% of the distance from the nose to the measurement point. Based on this location of transition, the estimated virtual starting point of turbulence occurs at approximately $x = 0.4D$. Using this virtual starting point of turbulence, the calculated flow parameters are $u_* = 0.363\,\text{m/s}$, $\delta = 8.6\,\text{cm}$, $\delta_* = 1.08\,\text{cm}$ and $\delta_\theta = 0.78\,\text{cm}$ and the resulting calculations of the spectra are shown in Fig. 7. Although not shown here, there were no appreciable differences when the data shown in Fig. 7 were compared to those calculated by assuming turbulence starts at the nose, since the measurement point is so far downstream from the nose. Because of the very thick boundary layer ($\delta_* = 1.08\,\text{cm}$), the spectral peak occurs at a very low frequency (when $\omega\delta_*/U_\infty \approx 0.2$), which is below the frequency range of available data, $0.5 \leqslant \omega\delta_*/U_\infty \leqslant 25$. The data in the peak and low-frequency regions are contaminated and not shown here. However, the universal range of the spectrum is well covered by available data.

3.3. Results of comparison between model predictions and measured data

The results of the comparison between the spectra predicted by the models and the corrected data obtained from measurements, shown in Figs. 3, 4, 6 and 7 are summarized as follows. For reference purpose, the experimental conditions for the data shown in these figures, and a few selected other experiments are compared in Table 1.

The Maestrello model [10] predicts a reasonably accurate mid-frequency spectrum, especially in and near the peak-frequency region. It overpredicts the low-frequency spectrum due to its slower roll-off from the peak (about $\omega^{0.6}$) in the low-frequency region. At frequencies above the peak frequency, the spectrum starts to roll off slowly and then increases gradually until the roll-off is proportional to ω^{-5}. However, this model does not characterize the distinct Reynolds number dependent feature in the universal range of the spectrum. Its predicted spectra matches well with low speed in-air data (Fig. 3), where data show no noticeable universal range. In high Reynolds number flows where the data have a large universal range (Figs. 4 and 7, for example), this model severely underpredicts the spectral level when $\omega\delta_*/U_\infty \gg 1$.

The spectra predicted by the Cockburn–Robertson [5] model differ completely from the data not only in the general spectral characteristics but also in levels. The most apparent shortcoming of this model is that there is no clear spectral peak, except that this model rolls off gradually at different rates from their respective maxima at zero frequency. This model, which was fitted to some specific high-speed flight test data, may not be applicable to different flow environments, especially in the very low-speed flow data used here (at Mach number nearly two orders of magnitude smaller).

The spectra predicted by the Efimtsov [12] are flat at frequencies below the spectral peak, and then transition to $\omega^{-10/3}$ behavior at high frequencies. It thus overpredicts the spectra below the peak frequency and does not show the typical peak region spectral behavior. Except for this drawback, the model's predicted spectra above the peak frequency agree reasonably well with data.

Using the integration limits discussed in Section 2.3, the spectra predicted by Witting's model [13] are close to that of the data near the peak region. Its predicted spectrum matches reasonably well with the low speed in-air data (Fig. 3). At higher speed, the predicted spectral levels in all other regions outside the peak region are generally much lower than the data. Although Witting's high- and low-frequency levels may be adjusted by using different integration limits, the authors were unable to find a suitable combination of limits that would yield a spectrum to match the data at all frequency ranges.

The spectra predicted by the Smol'yakov–Tkachenko model [17] are flat at frequencies below the spectral peak, and then transition to $\omega^{-7/3}$ behavior at high frequencies. Except in the very high Reynolds number flow, such as that shown in Fig. 7 ($R_x = 7.74 \times 10^7$), it overpredicts the spectra at low frequencies and mid frequencies. The predicted spectra are either too high or too low in the universal range due to the roll-off of $\omega^{-7/3}$ in this range.

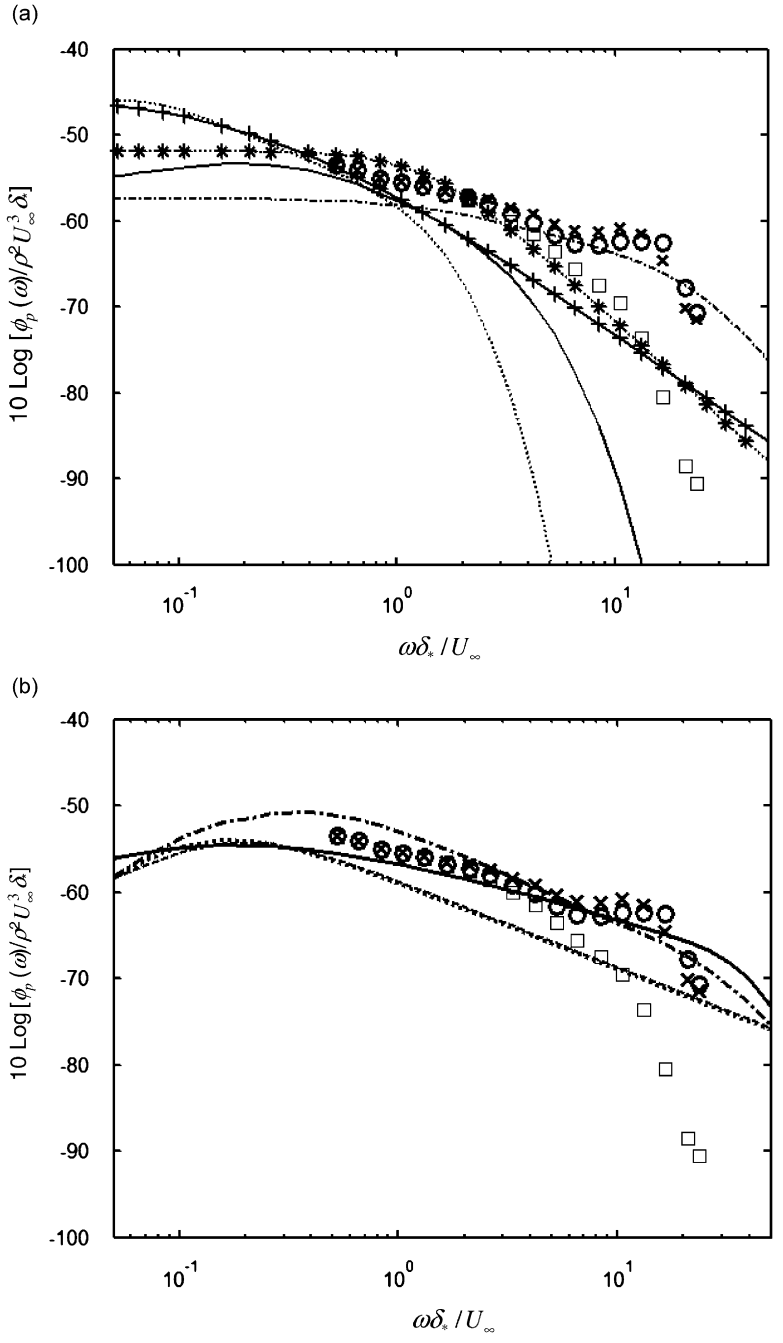

Fig. 7. Comparison of the underwater pressure spectrum measured at $R_x = 7.74 \times 10^7$ (with thick boundary layer, $\delta_* = 0.93$ cm) and predicted spectra calculated from the semi-empirical models. (a) Predicted spectra using model by (——) Maestrello, (—+—) Cockburn–Robertson, (—·—·—) Efimtsov, (·····) Witting and (···✚···) Smol'yakov–Tkachenko. (b) Predicted spectra using model by (– – – –) Chase, (▪▪▪▪▪▪) Chase–Howe, (—▪—▪—) Smol'yakov and (——) Goody. (○) the measured data corrected with Chase, (✖) measured data corrected with Corcos and (□) uncorrected measured data.

The spectra predicted using the Chase [14,15] and Chase–Howe [16] models agree well with the data in the mid-frequency region ($0.15 \leqslant \omega\delta_*/U_\infty \leqslant 0.6$, including the peak). In the universal range, the spectra predicted by the Chase and Chase–Howe models are lower (on the order of 1–6 dB) than the data due to the faster ω^{-1} roll-off as opposed to the $\omega^{-0.7}$ roll-off indicated by the data. In the high-frequency region, their predicted

Table 1
Measurement conditions for data shown in Figs. 3, 4, 6 and 7 and those for other authors

Figure no. or authors	Test facility	Fluid	U_∞ (m/s)	u_* (m/s)	δ (cm)	δ_* (cm)	θ (cm)	R_θ	a (mm)
3	Wind tunnel	Air	6.3	0.28	3.0	0.46	0.33	1.4×10^3	0.5
4	Wind tunnel	Air	15.5	0.625	2.79	0.45	0.33	3.39×10^3	0.395
6	Buoyant body	Water	20.6	0.7	0.74	0.1	0.07	12.2×10^3	1.5
7	Buoyant body	Water	12.9	0.363	8.6	1.08	0.78	70.5×10^3	1.27
Bull and Thomas [34][a]	Wind tunnel	Air	24.0	0.86	4.6	0.57	0.46	7×10^3	0.375
Carey et al. [35][a]	Pipe flow	Water	17.0	0.51	4.45	0.56	0.44	75×10^3	0.89
Keith and Bennett [36][a]	Channel flow	Water	6.1	0.2	1.88	0.23	0.20	13.4×10^3	1.0
Wilmarth and Wooldridge [37][a]	Wind tunnel	Air	47.6	1.58	11.4	1.16	1.04	29×10^3	2.07

[a]Measurement conditions extrapolated from the data tabulated by Keith and Bennett [36].

spectra substantially exceed the data due to their constant rate (ω^{-1}) of roll-off while the data roll off at faster rate, up to ω^{-5}. At low frequencies, the spectra predicted by the Chase model are higher while that predicted by the Chase–Howe model are lower than the data (only very limited data is available at low frequencies, e.g., Fig. 4).

At frequencies above the spectral peak, the spectra predicted by the Smol'yakov [8] model compare reasonably well with data. However, the model's predicted spectral peak frequency occurs at a considerably higher frequency than that of the data, and the predicted spectral levels below the peak frequency are significantly lower due to a larger range for the roll-off from the peak. This reflects the spectral peaks which occur at approximately $\omega\delta_*/U_\infty \approx 0.6$ in the data compiled by Smol'yakov [8] in his derivation of the model. Because the spectral peaks occur at higher frequencies, the predicted spectra in the universal range are generally higher than the data. However, due to the offset by its faster rate of roll-off ($\propto \omega^{-1.11}$) from the peak, the predicted spectra compare reasonably well with data at higher frequencies and in the upper frequency region of the universal range.

The spectra predicted by Goody's [9] model show good agreement with the data for all four cases, except the over-prediction in the low-frequency region of the first underwater case (see Fig. 6). The good agreement of the two in-air cases is no surprise, since Goody used these data to test his model. In the underwater cases, with the exception just mentioned, the agreement is also good even though Goody did not examine these data.

Overall, the most recent model developed by Goody [9] shows the best agreement with data of all models evaluated. This shows the gradual improvement of models over time. The newest models, such as Goody's, have benefited from additional information not available to the development of the earlier models.

As a check on the accuracy of the boundary layer parameters used, additional predictions were made using a range of different values. Different parameter values not only degrade the comparison of predictions with measured data but also make the predicted spectral peak frequency and the overall spectral levels shift away from the measured data. Therefore, the boundary layer parameters used in this comparison are believed to be reasonably accurate.

4. Conclusion

The results of the fluctuating wall pressure frequency spectra calculated using nine semi-empirical models were compared for the first time to four sets of data measured at different flow conditions: in-air and in-water, for flat and curved surfaces. The transducer size attenuation effects of the flush mounted sensors were computed using both Corcos's and Chase's wavenumber-frequency spectra. Measured data shown were those corrected by the calculated sensor size correction factors. Two sets of measured data are shown: one is corrected using the Corcos wavenumber spectrum and the other is corrected using the Chase spectrum. The uncorrected experimental data are also shown to indicate the amount of correction being made. In one of the four cases, the sensor was mounted beneath an elastomer blanket. In this case, the factor for the combined attenuations of the blanket and the sensor was used to correct the measured data.

The comparison between data and predictions for each of the models (either agreement or disagreement) are quite consistent for all cases evaluated. This suggests that the corrected data represent the actual point frequency spectra reasonably well.

The most recent model published by Goody [9] provides the best overall prediction of the frequency spectra for all cases evaluated. Goody used the Chase–Howe [16] model as the starting point for the development of his model. One of the changes by Goody on the Chase–Howe model is to have his model follow an $\omega^{-0.7}$ (instead of ω^{-1}) behavior in the universal range, which results in a better agreement with measured data on flat surfaces in air and to a lesser extent cylindrical surfaces underwater. This point is also supported by the smooth wall data of Blake [31], however the recent underwater data measured by Ciappi and Magionesi [32] suggest an ω^{-1} dependance. Despite this uncertainty, it appears that Goody has captured the spectral features correctly for turbulent boundary layer flows over a wide range of Reynolds number. The readers may use the information presented to choose a model appropriate for their specific applications.

Acknowledgment

This work was primarily funded by the Office of Naval Research (ONR Code 333, Dr. Kam Ng, the Scientific Officer) under Contract no. N00014-00-0058-17, from FY1999 to FY2003, while the first author was employed at Applied Research Laboratory, Pennsylvania State University. The encouragement and support provided by Dr. Ng are gratefully acknowledged. The financial assistance provided by the Electoacoustic Graduate Program at the College of Engineering, Feng Chia University is also gratefully acknowledged. The authors wish to thank the many useful suggestions provided by the two anonymous reviewers.

Appendix. A

A.1. Transmission of the normal surface traction across an elastomeric layer

The determination of the transmission of the normal surface traction across a fluid-loaded rigidly backed elastomeric layer shown by Fig. 8 can be conveniently derived using the formalism reported by Folds and Loggins [33], in which the state vectors of velocity and surface traction at the two free surfaces of a given elastic layer are related as follows:

$$\begin{bmatrix} v_x^{(2)} \\ v_z^{(2)} \\ Z_z^{(2)} \\ Z_x^{(2)} \end{bmatrix} e^{i(kx-\omega t)} = \begin{bmatrix} A_{11} & A_{12} & A_{13} & A_{14} \\ A_{21} & A_{22} & A_{23} & A_{24} \\ A_{31} & A_{32} & A_{33} & A_{34} \\ A_{41} & A_{42} & A_{43} & A_{44} \end{bmatrix} \begin{bmatrix} v_x^{(1)} \\ v_z^{(1)} \\ Z_z^{(1)} \\ Z_x^{(1)} \end{bmatrix} e^{i(kx-\omega t)} \tag{A.1}$$

where v and Z are the velocity and stress on the surfaces; the superscript, 1 or 2, indicates the surface location; and the subscripts x and z indicate the directions of the respective quantities; k (the symbol σ was used in Ref. [33]) is the wavenumber along the x-axis. The coefficients A_{ij} are functions of k, ω, the material properties (density, ρ_e; dilatational wave speed, c_l; and shear wave speed, c_s), and thickness, h, of the layer. The complete

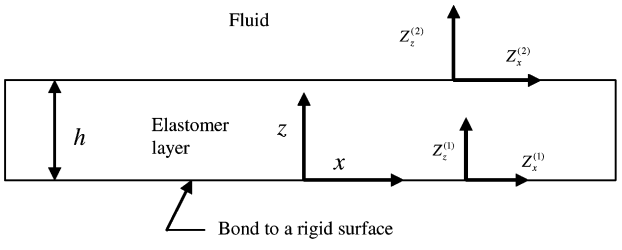

Fig. 8. A schematic of an elastomeric layer.

list of these coefficients can be found in Ref. [33]. Duplicating the expressions of these coefficients here is unnecessary since they will be substituted into the appropriate equations later and reflected in a final expression for the transmission coefficient.

Assuming Surface 1 is bounded to a rigid surface, $v_x^{(1)} = v_z^{(1)} = 0$, then Eq. (A.1) can be reduced to

$$Z_z^{(2)} = C_1 Z_z^{(1)}, \tag{A.2}$$

$$v_z^{(2)} = C_2 Z_z^{(1)}, \tag{A.3}$$

where $C_1 = A_{33} - A_{34}A_{43}/A_{44}$ and $C_2 = A_{23} - A_{24}A_{43}/A_{44}$. The two other expressions, for $v_x^{(2)}$ and $Z_x^{(2)}$, as dependent variables are not shown because they will not be used hereafter. Assuming the pressure on Surface 2 is caused by an incident velocity potential $\phi_I = B\mathrm{e}^{-\mathrm{i}\alpha_f z + \mathrm{i}kx - \mathrm{i}\omega t}$ of the fluid space above, Surface 2 will in general cause a reflected potential $\phi_R = A\mathrm{e}^{\mathrm{i}\alpha_f z + \mathrm{i}kx - \mathrm{i}\omega t}$. Here we use α_f to designate the z-axis wavenumber in the fluid medium and $k^2 + \alpha_f^2 = (\omega/c_f)^2$, where c_f is the sound speed in fluid. The amplitudes of the incident pressure and potential at Surface 2 are related by the following expression [33]:

$$P_{\mathrm{inc}} = \mathrm{i}\left(\frac{K}{\omega}\right)\left(\frac{\partial^2\phi_I}{\partial x^2} + \frac{\partial^2\phi_I}{\partial z^2}\right)_{z=h} = -\mathrm{i}\rho_f\omega B, \tag{A.4}$$

where K and ρ_f are the fluid bulk modulus and mass density, respectively. The normal surface velocity and stress are related to the sum of the potentials, i.e., $\phi = \phi_I + \phi_R$ and therefore,

$$v_z^{(2)} = \left.\frac{\partial\phi}{\partial z}\right|_{z=h} = \mathrm{i}\alpha_f(A - B) \tag{A.5}$$

and

$$Z_z^{(2)} = \mathrm{i}\left(\frac{K}{\omega}\right)\left(\frac{\partial^2\phi}{\partial x^2} + \frac{\partial^2\phi}{\partial z^2}\right)_{z=h} = -\mathrm{i}\rho_f\omega(A + B). \tag{A.6}$$

From Eqs. (A.2) to (A.6), the reflection coefficient A/B and subsequently the ratio $(A+B)/B$ can be obtained. Accordingly,

$$\frac{Z_z^{(2)}}{P_{\mathrm{inc}}} = \frac{A + B}{B} = \frac{2C_1}{C_1 + z_f C_2}, \tag{A.7}$$

where $z_f = \rho_f\omega[(\omega/c_f)^2 - k^2]^{-1/2}$ is the fluid impedance at Surface 2. The wall pressures are presumably measured on a rigid surface, so the wall pressure will be equal to two times the incident pressure. Substituting Eq. (A.2) into Eq. (A.7), and replacing P_{inc} by $2P_{\mathrm{inc}}$, we have the wall pressure transmission coefficient,

$$t = \frac{Z_z^{(1)}}{2P_{\mathrm{inc}}} == \frac{1}{C_1 + z_f C_2}. \tag{A.8}$$

Substituting the coefficient A_{ij} tabulated in Ref. [33], we have

$$t = \frac{\Upsilon\cos(P) + (1 - \Upsilon)\cos(Q)}{\Lambda + z_f\Phi}, \tag{A.9}$$

where

$$\Lambda = [(1 - \Upsilon)\cos(P) - \Upsilon\cos(Q)][\Upsilon\cos(P) + (1 - \Upsilon)\cos(Q)] + [\Delta\sin(P) - (\sigma/\beta)(1 - \Upsilon)\sin(Q)]^2,$$

$$\Phi = -i(k/\rho_e\omega)\left\{\begin{array}{c}[(\alpha/k)\sin(P) + (k/\beta)\sin(Q)][\Upsilon\cos(P) + (1 - \Upsilon)\cos(Q)] \\ -[\cos(P) - \cos(Q)][\Delta\sin(P) - (1 - \Upsilon)(k/\beta)\sin(Q)]\end{array}\right\},$$

$$\Delta = 2\alpha k c_s^2/\omega^2,\ \Upsilon = 2(kc_s/\omega)^2,\ \alpha^2 = (\omega/c_\ell)^2 - k^2,\ \beta^2 = (\omega/c_s)^2 - k^2,\ P = \alpha h,\ Q = \beta h$$

and c_l and c_s are the dilatational and shear wave speed of the solid layer, respectively.

References

[1] M.K. Bull, Wall pressure fluctuations beneath turbulent boundary layers: some reflections on forty years of research, *Journal of Sound and Vibration* 190 (3) (1996) 299–315.

[2] G.M. Corcos, Resolution of pressure in turbulence, *Journal of Acoustical Society of America* 35 (2) (1963) 192–199.

[3] W.R. Graham, A comparison of models for the wavenumber-frequency spectrum of turbulent boundary layer pressures, *Journal of Sound and Vibration* 206 (4) (1997) 541–565.

[4] W.K. Blake, *Mechanics of Flow-Induced Sound and Vibration*, Vols. I and II, Academic Press, New York, 1986.

[5] J.A. Cockburn, J.E. Robertson, Vibration response of spacecraft shrouds to in-flight fluctuating pressures, *Journal of Sound and Vibration* 33 (4) (1974) 399–425.

[6] T.M. Farabee, M.J. Casarella, Spectral features of wall pressure fluctuations beneath turbulent boundary layers, *Physics of Fluids A* 3 (1991) 2410–2420.

[7] W.L. Keith, D.A. Hurdis, B.M. Abraham, A comparison of turbulent boundary layer wall pressure spectra, *Journal of Fluid Engineering* 114 (3) (1992) 338–347.

[8] A.V. Smol'yakov, Calculation of the spectra of pseudosound wall pressure fluctuations in turbulent boundary layers, *Acoustical Physics* 46 (3) (2000) 342–347.

[9] M.C. Goody, Empirical spectral model of surface pressure fluctuations, *Journal of AIAA* 42 (9) (2004) 1788–1794.

[10] L. Maestrello, Radiation from panel response to a supersonic turbulent boundary layer, *Journal of Sound and Vibration* 10 (2) (1969) 261–295.

[11] B.M. Efimtsov, Characteristics of the field of turbulent wall pressure fluctuations at large Reynolds numbers, *Soviet Physics (Acoustics)* 28 (4) (1982) 289–292.

[12] B.M. Efimtsov, Similarity criteria for the spectra of wall pressure fluctuations in a turbulent boundary layer, *Soviet Physics (Acoustics)* 30 (1) (1984) 33–35.

[13] J.M. Witting, A spectral model of pressure fluctuations at a rigid wall bounding an incompressible fluid, based on turbulent structures in the boundary layer, *Noise Control Engineering Journal* 26 (1) (1986) 28–43.

[14] D.M. Chase, Modeling the wavevector-frequency spectrum of turbulent boundary layer wall pressure, *Journal of Sound and Vibration* 70 (1980) 29–67.

[15] D.M. Chase, The character of turbulent wall pressure spectrum at subconvective wavenumbers and a suggested comprehensive model, *Journal of Sound and Vibration* 112 (1) (1987) 127–147.

[16] M.S. Howe, *Acoustics of Fluid– Structure Interactions*, Cambridge University Press, Cambridge, 1998.

[17] A.V. Smol'yakov, V.M. Tkachenko, Model of a field of pseudosonic turbulent wall pressures and experimental data, *Soviet Physics (Acoustics)* 37 (6) (1991) 627–631.

[18] V.M. Tkachenko, V.P. Marshov, Normalization of the spectra of turbulent pressures by the outer and inner scales of a boundary layer, *Abstract of the Ninth Scientific-Technical Conference on Aircraft Acoustics (in Russian)*, Izd. Otd. TsAGI, Moscow, 1989, pp. 113–118.

[19] D.E. Capone, G.C. Lauchle, Calculation of turbulent boundary layer wall pressure spectra, *Journal of Acoustical Society of America* 98 (4) (1995) 2226–2234.

[20] G. Schewe, On the structure and resolution of wall pressure fluctuations associated with turbulent boundary layer flow, *Journal of Fluid Mechanics* 134 (1983) 311–328.

[21] T. M. Farabee, An experimental investigation of wall pressure fluctuations beneath non-equilibrium turbulent flows, David Taylor Research Center Technical Report No. 86/047, 1986.

[22] H.P. Bakewell, Turbulent wall-pressure fluctuations on body of revolution, *Journal of Acoustical Society of America* 43 (6) (1968) 1358–1363.

[23] H.D. Abarbanel, R.A. Katz, T.W. Cembrola, Nonlinear analysis of high-Reynolds-number flows over buoyant axisymmetric body, *Physical Review E* 49 (5) (1994) 4006–4018.

[24] T.A. Galib, R.A. Katz, S. Ko, B. Sandman, Attenuation of turbulent pressure fluctuations through an elastomeric coating. Technical Memorandum No. 912083, Naval Underwater Systems Center, Newport Laboratory, Newport, Rhode Island, 1991.

[25] A.E. Gentry, A.R. Wazzan, Transitional analysis program system, McDonnell-Douglas Research Report No. MDC J7255/02, 1976.

[26] H. Schlichting, *Boundary Layer Theory*, McGraw Hill, Inc., New York, 1979.

[27] K.L. Chandiramani, Response of underwater structures to convective component of flow noise, *Journal of Acoustical Society of America* 73 (3) (1983) 835–839.

[28] S.H. Ko, H.H. Schloemer, Flow noise reduction techniques for a planar array of hydrophones, *Journal of Acoustical Society of America* 92 (6) (1992) 3409–3424.

[29] C.H. Sherman, S.H. Ko, B.G. Buehler, Measurement of the turbulent boundary layer wave-vector spectrum, *Journal of the Acoustical Society of America* 88 (1) (1990) 386–390.

[30] M.J. Casarella, J.T.C. Shen, B.E. Bowers, On the evaluation of the axisymmetric forebody shapes for delaying laminar-turbulent transition—part 1: background and analysis of the problem, R & D Report 77-0074, David Taylor Naval Ship Research and Development Center, 1977.

[31] W.K. Blake, Turbulent boundary layer wall pressure fluctuations on smooth and rough walls, *Journal of Fluid Mechanics* 44 (1970) 637–660.

[32] E. Ciappi, F. Magionesi, Characteristics of the turbulent boundary layer pressure spectra for high-speed vessels, *Journal of Fluids and Structures* 21 (2005) 321–333.

[33] D.L. Folds, C.D. Loggins, Transmission and reflection of ultrasonic waves in layered media, *Journal of the Acoustical Society of America* 62 (5) (1977) 1102–1109.
[34] M.K. Bull, A.S.W. Thomas, High frequency wall-pressure fluctuations in turbulent boundary layers, *Physics of Fluids* 19 (4) (1976) 597–599.
[35] G.F. Carey, J.E. Chlupsa, H.H. Schloemer, Acoustic turbulent water-flow tunnel, *Journal of the Acoustical Society of America* 41 (2) (1967) 373–379.
[36] W.L. Keith, J.C. Bennett, Low frequency measurements of the wall shear stress and wall pressure in a turbulent boundary layer, *Journal of AIAA* 29 (4) (1991) 526–530.
[37] W.W. Willmarth, C.E. Wooldridge, Measurements of the fluctuating pressure at the wall beneath turbulent boundary layer, *Journal of Fluid Mechanics* 14 (2) (1962) 187–210.